Quasi-periodic Fibonacci and periodic one-dimensional hypersonic phononic crystals of porous silicon: Experiment and simulation

Gazi N. Aliev and Bernhard Goller

Citation: Journal of Applied Physics **116**, 094903 (2014); doi: 10.1063/1.4894620
View online: http://dx.doi.org/10.1063/1.4894620
View Table of Contents: http://scitation.aip.org/content/aip/journal/jap/116/9?ver=pdfcov
Published by the AIP Publishing

Quasi-periodic Fibonacci and periodic one-dimensional hypersonic phononic crystals of porous silicon: Experiment and simulation

Gazi N. Aliev[a] and Bernhard Goller[b]
Department of Physics, University of Bath, Bath BA2 7AY, United Kingdom

(Received 9 May 2014; accepted 23 August 2014; published online 5 September 2014)

A one-dimensional Fibonacci phononic crystal and a distributed Bragg reflector were constructed from porous silicon. The structures had the same number of layers and similar acoustic impedance mismatch, and were electrochemically etched in highly boron doped silicon wafers. The thickness of the individual layers in the stacks was approximately 2 μm. Both types of hypersonic band gap structure were studied by direct measurement of the transmittance of longitudinal acoustic waves in the 0.1–2.6 GHz range. Acoustic band gaps deeper than 50 dB were detected in both structures. The experimental results were compared with model calculations employing the transfer matrix method. The acoustic properties of periodic and quasi-periodic structures in which half-wave retarding bi-layers do not consist of two quarter-wave retarding layers are discussed. The strong correlation between width and depth of gaps in the transmission spectra is demonstrated. The dominant mechanisms of acoustic losses in porous multilayer structures are discussed. The elastic constants remain proportional over our range of porosity, and hence, the Grüneisen parameter is constant. This simplifies the expression for the porosity dependence of the Akhiezer damping.
 [http://dx.doi.org/10.1063/1.4894620]

I. INTRODUCTION

Phononic crystals, like photonic crystals, are of increasing scientific interest mainly due to the existence of frequency gaps, where propagation of elastic waves in the crystal is fully suppressed. Phononic crystals are widely applied as thermal barriers, elastic/acoustic filters, acoustic lenses, waveguides, mirrors, and sound-protection devices (see e.g., review by Steurer *et al.*[1]). Acoustic mirrors and filters operating in the GHz region, for instance, are of great importance in acoustoelectronic devices used in modern communication systems.[2]

1D phononic crystals consist of multilayers with periodically or aperiodically alternating thickness and acoustic impedance. A structure is said to be aperiodic if it lacks translational symmetry. A quasi-periodic structure is an aperiodic structure that nevertheless possesses some form of spatial ordering. In a 1D quasi-periodic structure, this ordering is due to a rule that generates the structure. As a result, these quasi-periodic structures exhibit spectral gaps in the frequency domain, which give an extra degree of freedom for tailoring phononic and photonic band gaps.[3] For example, a Fibonacci 1D quasicrystal is a more preferable candidate than a periodic Bragg structure for constructing omnidirectional photonic band gaps.[4] The creation of waveguides and cavities can profit from the isotropy and the assumed defect insensitivity of quasiperiodic metacrystals[1] (see also in Ref. 1, the review of the applications of the quasiperiodic structures). Hybrid structures—periodic structures combined with aperiodic ones—have been reported to be effective for tuning resonance transmission modes.[5]

In periodic 2D and 3D phononic and photonic crystals, the spectral gaps are usually called pseudo-gaps if they are not omnidirectional. Further, in a quasi-periodic structure, the gaps have been also termed pseudo-gaps due to the lack of translational symmetry.[6] However, for brevity, we shall not make this distinction between gaps and pseudo-gaps in this paper.

Recent experimental work[7–10] shows that porous silicon (PSi) is a promising material for phononic and phoxonic (simultaneous phononic and photonic gaps) applications. Porosity (fractional volume of voids) determines density and acoustic velocity and can be varied for PSi from 4% to 95%. For mesoporous PSi (a pore size ~2–50 nm), it has been shown[11] that the acoustic longitudinal velocity varies from ~7 km/s to ~1 km/s for 25% to 85% porosity, respectively. This allows one to fabricate hypersonic phononic structures in commercially available Si wafers.

Optical properties of PSi based 1D quasicrystals such as reflectance,[12–14] transmittance,[12,15,16] and photoluminescence[12] have been reported in the literature. For PSi based passive optical devices, e.g., multilayers for optical filtering or sensing applications,[17,18] knowledge of the refractive index calculated from the porosity is normally sufficient to characterize a sample or its constituent layers. This is the case because the effective medium method for the dielectric constant depends predominantly on the porosity (i.e., density) of a layer with only a weak dependence on the micromorphology.[19] In contrast, for acoustic devices, e.g., a PSi Bragg reflector or a rugate filter,[8–10] the characteristic impedance of an acoustic layer, $Z = \rho v$, depends on the density ρ of the layer and the acoustic velocity v, which depends, in turn, on the porosity and morphology of the layer.[11]

[a]Author to whom correspondence should be addressed. Electronic mail: g.aliev@bath.ac.uk
[b]Present address: Infineon Technologies AG, Siemensstrasse 2, 9500 Villach, Austria.

Therefore, optical characterization of structures designed for acoustic applications alone does not give information sufficient to predict the acoustic properties of the structures. Also, optical devices working in the visible and near-infrared regions usually have a lattice spacing an order of magnitude less than the acoustic superlattices designed for the hypersonic (GHz) region. The overall thickness of optical multilayers is usually smaller, which makes fabrication easier.

In optics, the speed of light in the porous material in the effective medium approximation is equal $v_{op} = c/n_{eff}$, where c is speed of light in a vacuum and n_{eff} is the effective refractive index of the material. In acoustics, there is no such simple relationship. There are various semi-empirical models for the porosity dependence of the velocity (or elastic constants) of porous materials (see review of the models in Refs. 20 and 21). These have been used to calculate acoustic velocities through porous rocks[21] and composite materials.[22] In this work, we discuss a new formula, which is a modification of the well known formula,[22] by considering the effect of multiple scattering (Sec. III A).

The other difference between optical and acoustic waves propagating through a material is the mechanism of losses. While scattering by surface and interface roughness,[23–27] and Rayleigh or multiple scattering by voids[28–30] in optics and acoustics can be described by almost the same formalism, the mechanism of light absorption within a layer is completely different from the mechanism of acoustic damping. In Sec. III F, we discuss the dominant mechanism of viscous acoustic damping and its dependence on porosity.

Ageing effects, e.g., oxidation in air, are noticeable[31,32] for optical properties of PSi based devices as silica has significantly different optical properties from silicon: $n_{Si}/n_{SiO_2} \approx 2.7$. In contrast, silica and silicon have a smaller difference in acoustic properties: $v_{Si}/v_{SiO_2} \approx 1.4$ and $Z_{Si}/Z_{SiO_2} \approx 1.5$. Bellet *et al.*[33] concluded that oxidation did not significantly change the Young's modulus of PSi samples and almost no effects of ageing were observed to cause changes in the transmission spectra of an acoustic superlattices.[8] Therefore, the acoustic properties obtained from optical characterization of the freshly fabricated and the aged sample may be inconsistent.

In spite of all the differences mentioned, at normal incidence of acoustic wave, the optical methods can be applied for simulation of acoustic wave propagation through a multilayered structure. By just changing a scaling factor, acoustic devices can be designed in the same way as optical devices (Secs. III D and III C).

In the present work, we report fabrication of a quasi-periodic one-dimensional Fibonacci phononic crystal of PSi and its acoustic spectrum for longitudinal waves. A Fibonacci quasicrystal is a structure (FS) that is formed by stacking two layers A and B with different impedances according to the Fibonacci sequence generation scheme: $(\mathrm{FS})_L = \{F_0 F_1 F_2 \cdots F_L\}$, where $F_0 = A$, $F_1 = B$, $F_2 = AB$, $F_3 = BAB$, $F_4 = ABBAB$, …, $F_L = \{F_{L-2}, F_{L-1}\}$. This is equivalent to iterated application of the substitutional rule: $A \rightarrow B$, $B \rightarrow AB$. We shall note that, for odd L, $(\mathrm{FS})_L = \{B\ F_{L+2}\}$ and, for even L, $\{A\ (\mathrm{FS})_L\} = \{AB\ F_{L+2}\}$. Here, we discuss the acoustic measurements an FS with $L = 7$, which consists of 21 A-layers and 33 B-layers of PSi on a bulk Si substrate: ABABBABABBABABABBABABBABABABBABABBABABABBAB.

In this work, we also study a periodic Bragg structure (BS) consisting of 27 pairs of AB layers of nearly the same thickness and impedance mismatch as for the FS. Phononic properties of both types of multilayered structures correlate strongly:[34] the spectral gaps of the FS are distributed about the central frequency of the band gap of the corresponding BS.

Most of the work in the literature considers periodic and aperiodic structures comprising of AB layers in which A-layer and B-layer are both quarter-wave retarding. Here, we discuss some properties of the structures in which half-wave retarding bi-layers do not consist of two quarter-wave retarding layers (Secs. III C and IV H).

Our work aims to illustrate the different characteristics of the FS and BS. We provide a novel analysis which we feel will aid other workers to chose between the two types of structure and design them appropriately.

II. EXPERIMENTAL

PSi multilayers were fabricated using electrochemical etching.[17] The wafer material used was highly-boron-doped CZ silicon with a resistivity of 0.001–0.005 Ωcm and a thickness of 525 μm cut in the (100) plane. Room temperature anodization was performed in a 1:1 solution of 48% aqueous-HF and ethanol. High- and low-porosity layers were obtained by alternating the current density in the range 100–150 mA/cm^2. The thickness of the layers was controlled by the etching duration. Figure 1 shows scanning electron microscope (SEM) images of cross-sections of the fabricated BS (a) and FS (b). Thicknesses of the A and B layers were assessed using the results of SEM measurement, and were found to be constant throughout the whole structure with an uncertainty of ~0.06 μm (see more details in Sec. IV).

To characterize the etched structures acoustically, the acoustic transmission spectra (ATS) were recorded using the experimental technique shown schematically in Figure 2. A

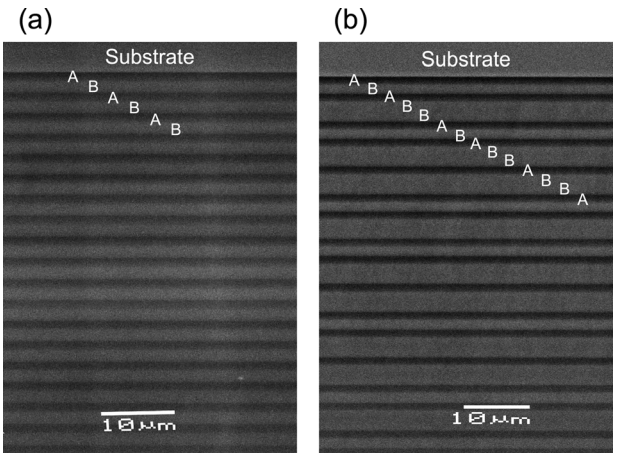

FIG. 1. SEM cross sections of fragments of (a) the BS (first 36 layers from 54) and (b) the FS (first 41 layers from 54). High and low porosity layers are depicted by A and B, respectively. The layers with higher porosity appear darker. The overall thickness was measured to be ~109 μm for the BS and ~115 μm for the FS. Scale bars are shown in each micrograph.

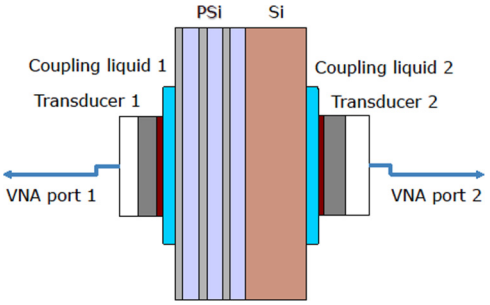

FIG. 2. Schematics of the experimental setup used for the acoustic transmission measurements.

specimen was placed between two transducers operating with the maximum efficiency at 1 GHz. Each transducer consists of a ZnO piezoelectric layer driving waves into a square silicon pillar $160\,\mu m \times 160\,\mu m \times 520\,\mu m$ with a thin ($0.5\,\mu m$) SiO_2 antireflection coating. Transducers were coupled to the specimen via water or liquid In-Ga eutectic. Acoustic waves were emitted into the PSi layers with normal incidence (less than 0.5° uncertainty in alignment). The transducers were connected to 2-ports of a vector network analyzer (VNA) and the signal transmitted through the structure was measured as an S_{21}-parameter with sweeps performed from 0.1 to 2.6 GHz with a bandwidth of 100 Hz and a resolution of 1.5 MHz. The magnitude of *S*-parameters (scattering parameters) are determined by measuring the magnitude of the incident, transmitted, and reflected voltage signals V_{in}, V_t, and V_r, respectively:[35] $S_{11} = V_r/V_{in}$, $S_{21} = V_t/V_{in}$.

For the Si wafer and etching conditions employed for our measurement, the pore shape was something between a right prism and a cylinder with distribution of pore radius $a \sim 5$–20 nm and an aspect ratio $\zeta \sim 1-4$ (see e.g., Refs. 17 and 36). The velocity dependence on porosity, i.e., κ-parameter (see Sec. III A), was experimentally determined for PSi single layers from acoustic Fabri-Perot interference spectra recorded in the same frequency range using the same experimental technique as described above (see details in Refs. 11 and 37). The parameter κ obtained was 0.585 ± 0.030. For the PSi layers etched at similar conditions, this value within the frame of an experimental error was validated by the several works: 0.595 (Ref. 9), 0.58 ± 0.03 (Refs. 11 and 37), 0.62–0.76 (Ref. 38), and 0.560 ± 0.015 (Ref. 39).

III. THEORY

A. Acoustic velocity in PSi

The density ρ and the acoustic velocity v in PSi are functions of porosity ϕ and can be expressed as[11]

$$\rho = \rho_0(1-\phi), \tag{1}$$

$$v = v_0(1-\phi)^{\kappa-\delta}/\Re\{(1-b\phi)^{1/2}\}, \tag{2}$$

where ρ_0 and v_0 are the density and the acoustic velocity of bulk Si, respectively (see Table II), κ is a fitting parameter, $b = \psi(A + Bk_1^2a^2 - iCk_1^3a^3)$, where ψ is 1, ζ^{-1}, $\frac{2}{3}\zeta^{-1}$ and $\frac{\pi}{6}\zeta^{-1}$ for voids with the spherical, ellipsoidal, cylindrical, and right-prism shape, respectively, ζ is aspect ratio of pores, a is the pore radius, A, B, and C are the Sayers' coefficients depending on the ratio of longitudinal (v_L) and shear (v_S) wave velocities (see Appendix), and $k_1 = \omega/v_1$, where $v_1 = v_0(1-\phi)^{\kappa-\delta}$. The parameter $\delta = -\frac{1}{2}\ln(1-b_1\phi_1)/\ln(1-\phi_1)$, where $b_1 = \psi A$, is introduced to make Eq. (2) consistent with the similar but simpler equation commonly used in the literature[22,37–41]

$$v = v_0(1-\phi)^{\kappa}, \tag{3}$$

such that Eqs. (2) and (3) with the same κ intersect at $\phi = \phi_1$. In this work, we used $\phi_1 = 0.5$.

As a consequence of the assumptions made in Ref. 11 about porosity dependence of v_L and v_S, the ratio v_L/v_S is independent of porosity and equal to 1.44 for PSi. Thus, the Sayers' coefficients are independent of porosity and for PSi are: $A \approx -0.919$, $B \approx -1.86$, and $C \approx 2.16$.

The acoustic velocity dispersion induced by the effect of multiple scattering[28–30] is also included in Eq. (2), though, for $ka \ll 1$, it can be neglected with $b \approx \psi A$, thus the term $(1-b\phi)^{1/2}$ is always real, and there is no need to use a as a fitting parameter. We shall note that in bulk Si, the velocity dispersion is negligible.[42,43]

As it is seen from Eqs. (2) and (3), increasing porosity ϕ and increasing the κ-parameter lead to decreasing acoustic velocity v in PSi. Note that Eqs. (2) and (3) are valid in the effective medium approximation when the pore size is smaller than the acoustic wavelength. For mesoporous PSi multilayers studied in our work at the GHz range, this limit is well fulfilled: $ka < 0.03$.

B. Fibonacci structure

Though the FS is constructed by stacking two (A and B) types of layer, physically, there are three types of layer in the FS: A-type layers and two B-type layers: a single thickness (B′) and a double thickness (B″) (see Figure 1(b)). The number of B-letters in a Fibonacci word is: $N^B = N^{B'} + 2N^{B''}$, where the upper index corresponds to the type of layer. Clearly, the number of A-type layers is equal to the number of B-type layers: $N^A = N^{B'} + N^{B''}$. Further, N^A in the FS of any L is equal to the L-th member of the *natural* Fibonacci sequence whereas N^B, $N^{B'}$ and $N^{B''}$ are equal to the L-th members of the natural *Fibonacci-like* sequences given in Table I. Thus, for $L = 7$, we have $N^{B'} = 9$ and $N^{B''} = 12$.

C. Distributed Bragg reflector

1. Position and width of forbidden gaps

In optics, a BS consists of a number of repeated layer pairs where each pair consists of a layer of thickness d_A

TABLE I. Number of layers in Fibonacci structures of different *L*.

L	0	1	2	3	4	5	6	7	8	9	10	…	L
N^A	1	1	2	3	5	8	13	21	34	55	89	…	$N_{L-1}+N_{L-2}$
N^B	0	1	2	4	7	12	20	33	54	88	143	…	$N_{L-1}+N_{L-2}+1$
$N^{B'}$	0	1	2	2	3	4	6	9	14	22	35	…	$N_{L-1}+N_{L-2}-1$
$N^{B''}$	0	0	0	1	2	4	7	12	20	33	54	…	$N_{L-1}+N_{L-2}+1$

TABLE II. Acoustic properties of coupling liquid and transducer materials.

	ρ (g/cm^3)	v_L (km/s)	v_S (km/s)	α/f^2 (dB cm^{-1}GHz^{-2})
Ga-In	6.35[a]	2.74[a]	0	137[b]
Si	2.329[c]	8.4332[d]	5.8446[d]	9.32[e]
SiO_2	2.150[c]	5.968[c]	3.764[c]	4.46[f]
ZnO	5.606[c]	6.400[c,g]	2.950[c,g]	13.6[h]

[a]Reference 50.
[b]Reference 53, (liquid Ga).
[c]Reference 51.
[d]Reference 52.
[e]Reference 54.
[f]Reference 55.
[g]c-axis.
[h]Reference 56.

having refractive index n_A followed by a layer of thickness d_B with index n_B. The reflectivity of the structure is determined by the number of repeating pairs and by the refractive index contrast between the layer materials. The strong reflectivity profile—the optical band gap—appears around the Bragg wavelength (in vacuum), λ_{Br}, given for normal incidence by: $m\lambda_{Br}/2 = d_A n_A + d_B n_B$, where $m(= 1, 2, 3\ldots)$ is the order number for the multiple stop bands. This can be rewritten as: $mc/2f_{Br} = d_A c/v_A + d_B c/v_B$, where f_{Br} is the Bragg frequency and $v_{A(B)}$ is the speed of light in the layer material. In this form, the Bragg condition can be applied for acoustic waves. Thus, for the BS, the center frequency of the stop bands f_{Br} of different order m, for normal incidence, can be expressed as

$$f_{Br}^{(m)} = m/2t, \tag{4}$$

where $t = t_A + t_B$, $t_A = d_A/v_A$, $t_B = d_B/v_B$, and $v_{A(B)}$ is the acoustic velocity of the layers. The corresponding gap widths Δf^b for odd and Δf^c for even m can be expressed following Ref. 44 as

$$\begin{aligned} \Delta f_m^b &= \frac{2}{\pi t}\left|M\cos\left(\frac{\pi m\, t'}{2t}\right)\right|, \; m = 1, 3, 5\ldots, \\ \Delta f_m^c &= \frac{2}{\pi t}\left|M\sin\left(\frac{\pi m\, t'}{2t}\right)\right|, \; m = 2, 4, 6\ldots, \end{aligned} \tag{5}$$

where $M = (Z_A - Z_B)/(Z_A + Z_B)$ and $t' = t_A - t_B$.

As follows from Eq. (5), the widths of the gaps change with increasing m in a complex manner depending on the ratio t'/t. In special cases, when $t_{A(B)} = p\, t_{B(A)}$, where p is an integer, the gaps of the order $m = q(p+1)$, where $q = 1, 2, 3\ldots$, are missing. For instance, when $p = 1$, i.e., $t_A = t_B$ and $t' = 0$, all gaps with even m disappear and the widths of all gaps with odd m become equal. Such structures, where the alternating A and B layers are both quarter-wave retarding with $t_A = t_B = 1/4f_{Br}^{(1)}$, we call "balanced." Thus, for the balanced BS, there are no even-order stop bands. In the other special case, when $p = 2$, i.e., $t_B = 2t_A$, $t' = t_A$, all gaps with $m = 3, 6, 9\ldots$ collapse and the widths of all remaining gaps are equal. However, when $p = 3$, i.e., $t_B = 3t_A$, $t' = 2t_A$, and all gaps with $m = 4, 8, 12\ldots$ collapse, there will be two types of gaps with different width (and, thus, depth): narrower for orders $m = \{1, 3\}q$ and wider for orders $m = 2q$. In general, there will be a sequence of $n = \lceil p/2 \rceil$ types of gap with gap-width increasing with n for orders

$$m = \{1, p\}q,\ \{2, p-1\}q, \ldots, \{n, p-n+1\}q. \tag{6}$$

The FS, strictly speaking, cannot be balanced in the same way as the BS: if $t_A = t_B$, then $t_{B''} = 2t_A$. However, when BS gaps of certain orders collapse, the corresponding FS gaps, spacing around the BS gaps, also collapse. Interestingly, the center frequencies of the dominant FS gaps, as demonstrated in Figure 4(b), nearly coincide with the center frequencies calculated for the periodic AB'' structure.

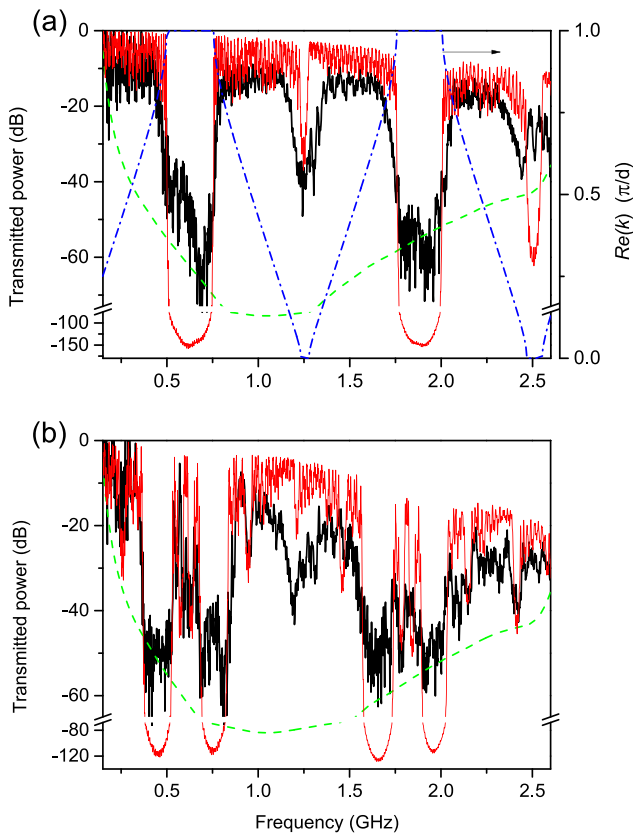

FIG. 3. Measured (thick black line) and calculated (thin red line) spectra of acoustic wave transmission through (a) the BS and (b) the FS on bulk Si substrates with porosity and thickness of A and B layers given in the text. The transmittance (log power in dB) is normalized to its maximum and corrected for transducer response. The longitudinal modes of the transducer and the coupling liquid, and the acoustic losses are included into the calculation. The dashed green line shows the detecting limit of the experimental system. For (a), right scale: the dash-dot blue line is the reciprocal wavevector k (real values) in units of π/d calculated using Eq. (11).

2. Depth of the gaps

The value of the center gap transmittance T_{Br} in the balanced BS consisting of $N = N^A + N^B$ quarterwave-layers, without attenuation considered, can be estimated following Ref. 45 as

$$T_{Br} = \frac{4\chi}{(1+\chi)^2}, \tag{7}$$

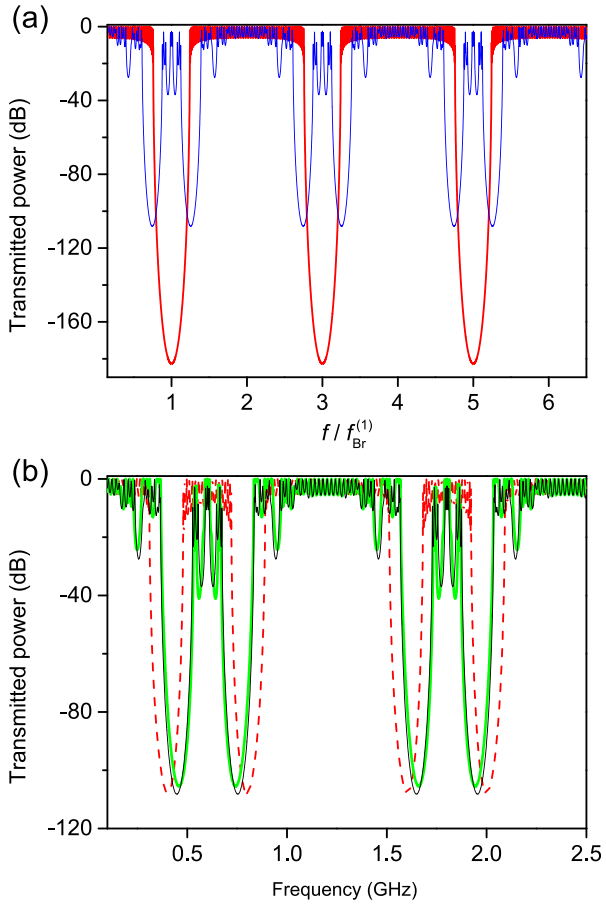

FIG. 4. (a) The simulated ATS of the BS (28 pairs), thick red line, and the FS ($L=7$), thin blue line. The layer porosity and thicknesses for both structures are: $\phi_A = 0.69$, $\phi_B = 0.49$, $d_A = 1.792\,\mu$m, and $d_B = 2.367\,\mu$m. Overall thicknesses of both structures are $\sim 116\,\mu$m. The acoustic losses and the effects of transducers, substrate, and coupling liquids are not included. (b) The simulated ATS of the FS as in (a), thin black line, the periodic structures $\{AB''\} \times 19$ with overall thickness of $124\,\mu$m, dashed red line, and $\{AB'AB''AB'AB''AB''\} \times 4$ with overall thickness of $112\,\mu$m, thick green line.

where $\chi = \frac{Z_{in}}{Z_{sub}}\left(\frac{Z_A}{Z_B}\right)^N$, and Z_{in} and Z_{sub} are the acoustic impedances of the incident and substrate media, respectively. To estimate the center gap transmittance for the unbalanced BS, we suggest Eq. (7) with modified $\chi \to \chi'$:

$$T_{Br}^{(m)} \approx \frac{4\chi'}{(1+\chi')^2}, \tag{8}$$

where

$$\chi' = \frac{Z_{in}}{Z_{sub}}\left(\frac{1+M'}{1-M'}\right)^N, \tag{9}$$

and

$$M' = \begin{cases} \left|M\cos\left(\dfrac{\pi m\, t'}{2t}\right)\right|, & m = 1,3,5\ldots \\ \left|M\sin\left(\dfrac{\pi m\, t'}{2t}\right)\right|, & m = 2,4,6\ldots. \end{cases} \tag{10}$$

From Eq. (7), $M' = \pi t \Delta f/2$. The expected center gap reflectivity is $R_{Br}^{(m)} = 1 - T_{Br}^{(m)}$.

3. Folded phonons

Eq. (5) is derived by the authors of Ref. 44 in the framework of Rytov's model.[46] The model gives a relation between the normal components of the phonon wavevectors of individual layers k_A and k_B and the wavevector of the superlattice k, assuming an infinite number of AB pairs

$$\cos(kd) = \cos(k_A d_A)\cos(k_B d_B) - \frac{1}{2}\left(\frac{\eta_A}{\eta_B} + \frac{\eta_B}{\eta_A}\right)\sin(k_A d_A)\sin(k_B d_B), \tag{11}$$

where $d = d_A + d_B$. Non-zero imaginary values of k correspond to the frequencies of forbidden gaps.

D. Transfer matrix method

The ATS have been modeled using a generalized matrix method given by Mitsas and Siapkas[26] for optical wave propagation through a multilayered structure. At normal incidence, this method can be used for acoustic waves by replacing the optical wave number with the acoustic wave number $k = \omega/v$, where v is the sound velocity (shear or longitudinal) and $\omega = 2\pi f$ is the angular frequency, and by replacing optical admittance, i.e., refractive index, with the parameter $\eta = (k\varkappa)^{-1}$, where $\varkappa$ is a stiffness constant.[47,48] For waves propagating in the [100] direction of a material with cubic symmetry, $\varkappa_L = c_{11} = \rho v_L^2$ for longitudinal acoustic waves and $\varkappa_S = c_{44} = \rho v_S^2$ for shear waves.[11] As one can see, $\eta^{-1} = \omega Z$, where $Z = \rho v$ is the characteristic acoustic impedance. The acoustic potential $\varphi = P/\rho\omega^2$, where P is acoustic pressure, in the incident (in) and output ($N+1$) media (assuming them to be infinite) can be expressed for longitudinal plane waves propagating in the z-direction as[49]

$$\begin{aligned} \varphi_{in}(z,\omega,t) &= (A_{in}^{+}e^{izk_{in}} + A_{in}^{-}e^{-izk_{in}})e^{-i\omega t}, \\ \varphi_{N+1}(z,\omega,t) &= A_{N+1}^{+}e^{i(zk_{N+1}-\omega t)}, \end{aligned} \tag{12}$$

where t is time, k_{in} and k_{N+1} are the wavenumbers of the incidence and output media, respectively, A_{in}^{+}, A_{in}^{-}, and A_{N+1}^{+} are the amplitudes of waves propagating in the positive (+) and negative (−) directions of the z-axis. These amplitudes are connected to each other by the system of equations[26]

$$\begin{pmatrix} A_{in}^{+} \\ A_{in}^{-} \end{pmatrix} = G\begin{pmatrix} A_{N+1}^{+} \\ A_{N+1}^{-} \end{pmatrix}, \tag{13}$$

where G is called the system transfer matrix. The amplitude A_{N+1}^{-} is equal to zero while wave incidence is considered only from one side. Reflectance and transmittance are defined as $\mathbf{r} = A_{in}^{-}/A_{in}^{+}$ and $\mathbf{t} = A_{N+1}^{+}/A_{in}^{+}$, respectively. G is obtained by consecutive multiplication of reflective (W) and phase (U) matrices for each interface and layer in the multilayered structure consisting of N layers:

$$G = W_{0/1}U_1W_{1/2}U_2\ldots W_{N/N+1} = \begin{pmatrix} G_{11} & G_{12} \\ G_{21} & G_{22} \end{pmatrix}. \tag{14}$$

The index 0 here corresponds to the incidence medium.

The reflective matrix for the interface between the $(j-1)$-th and j-th layers is given as

$$W_{j-1/j} = \frac{1}{t_j^+}\begin{pmatrix} 1 & -r_j^- \\ r_j^+ & t_j^+ t_j^- - r_j^+ r_j^- \end{pmatrix}, \tag{15}$$

where

$$r_j^+ = \frac{\eta_{j-1} - \eta_j}{\eta_{j-1} + \eta_j},\ r_j^- = -r_j^+,\ t_j^+ = 1 - r_j^+,\ t_j^- = 1 - r_j^-.$$

The phase matrix for the j-th layer is given as:

$$U_j = \begin{pmatrix} e^{ik_j d_j} & 0 \\ 0 & e^{-ik_j d_j} \end{pmatrix}, \tag{16}$$

where k_j and d_j are the z-component of the wavevector and the thickness of the j-th layer, respectively.

From Eq. (13),

$$\mathbf{r} = G_{21}/G_{11},\ \mathbf{t} = 1/G_{11}. \tag{17}$$

The power reflectance and transmittance are obtained as magnitudes of the complex vectors $\mathbf{r}$ and $\mathbf{t}$, respectively

$$R = \mathbf{r}^*\mathbf{r},\ T = \frac{Z_{in}}{\Re\{Z_{N+1}\}}\mathbf{t}^*\mathbf{t}, \tag{18}$$

where the asterisk denotes complex conjugate and Z_{in} and Z_{N+1} are acoustic impedances of input and output media, respectively.

Without including the effect of transducers into the calculation, left and right half-spaces were Ga-In liquid. The effect of transducers was included by adding a 520 μm thick Si layer followed by a $\sim$0.4 μm thick SiO_2 layer to both sides of the structure, symmetrically. ZnO was taken to be the material of left and right half-spaces, and coupling liquid was taken to be the layer with finite thickness ($\sim$1–50 μm). The acoustic properties of ZnO, SiO_2, and Ga-In eutectic are given in Table II.

The described transfer matrix method was chosen for our numerical calculations because of its convenience in including wave scattering by interface roughness. We have to note that the method is not valid for calculation of reflection and transmission coefficients of acoustic waves in solid at oblique incidence. The appropriate method[49,57,58] must be used in that case.

E. Scattering by interface roughness

Interface roughness can be considered by modification of quantities given in Eq. (15) as[23–27]

$$\begin{aligned} \tilde{r}_j^+ &= r_j^+ e^{-2k_{j-1}^2\sigma_j^2}, \\ \tilde{r}_j^- &= r_j^- e^{-2k_j^2\sigma_j^2}, \\ \tilde{t}_j^+ &= t_j^+ e^{-\frac{1}{2}(k_{j-1}-k_j)^2\sigma_j^2} \\ \tilde{t}_j^- &= t_j^- e^{-\frac{1}{2}(k_j-k_{j-1})^2\sigma_j^2}, \end{aligned} \tag{19}$$

where σ_j is the roughness (the root mean square deviation of the surface to the planarity) of the $(j-1)/j$ interface.

F. Acoustic losses within a layer

Attenuation can be included by making the wavenumber of an attenuating layer complex,[29] such that $\tilde{k} = k - i\alpha$, where α is an attenuation coefficient of the layer (the index j is omitted for brevity). The acoustic impedance of the attenuating layer also becomes complex. With the definition of attenuation given, the complex impedance of the layer is

$$\tilde{Z} = \rho\omega/\tilde{k} = Z(1 + i\varepsilon)/(1 + \varepsilon^2), \tag{20}$$

where $\varepsilon = \alpha/k$ is an extinction coefficient of the layer.

The attenuation coefficient α can be split to two components depending on the mechanism of acoustic losses: $\alpha = \alpha_{att} + \alpha_{sca}$, where $\alpha_{att} \propto \omega^2$ corresponds to the acoustic losses due to viscous damping, and $\alpha_{sca} \propto \omega^4$ corresponds to the acoustic losses in porous material due to multiple scattering by voids.

1. Akhiezer damping

At finite temperatures, there exists in all materials an equilibrium distribution of thermally-excited phonons. Propagating acoustic waves disturb this phonon equilibrium, with a resulting energy loss. This loss mechanism is known as Akhiezer damping, which is assumed to be dominant in semiconducting materials.[59,60] The slightly simplified formula for Akhiezer damping (see detailed discussion in Ref. 60) is given as[61]

$$\alpha_{att} = \frac{3\bar{\gamma}^2 KT\omega^2}{\rho\bar{v}^2 v^3}, \tag{21}$$

where $\bar{\gamma}$ is the averaged Grüneisen parameter, $\bar{v}^{-3} = (v_L^{-3} + 2v_S^{-3})/3$ is the Debay average velocity,[60] K is the thermal conductivity, T is the temperature, and v is the velocity (v_L or v_S) of the propagating wave. The effective thermal conductivity of PSi can be expressed as[62]

$$K = K_0(1 - \phi)^{\beta+1} \tag{22}$$

where $\beta = 1.3 - 2$ is a parameter depending on the morphology of PSi and K_0 is the thermal conductivity of bulk Si. The ratio of attenuation coefficients of PSi and bulk Si can be written as:

$$\frac{\alpha_{att}}{\alpha_0} = \frac{\bar{\gamma}^2}{\bar{\gamma}_0^2}\frac{K}{K_0}\frac{\rho_0}{\rho}\frac{\bar{v}_0^2}{\bar{v}^2}\frac{v_0^3}{v^3}. \tag{23}$$

As discussed in Refs. 63 and 64, $\bar{\gamma} \approx \frac{3}{2}(c_{11} + 2c_{12})/(c_{11} + 2c_{44})$, where c_{ij} are elastic constants. The assumption that the elastic constants remain proportional over our range of porosity[11] implies that $\bar{\gamma}$ is independent of porosity: $\bar{\gamma}/\bar{\gamma}_0 = 1$. The acoustic velocities v_L and v_S also depend on ϕ in the same functional form (Eq. (2)), thus $\bar{v}_0/\bar{v} = v_{0S}/v_S = v_{0L}/v_L$. Therefore, the attenuation in a porous layer with respect to the attenuation in a layer of zero porosity can be written as:

$$\alpha_{att} \approx \alpha_0\frac{K}{K_0}\frac{\rho_0}{\rho}\left(\frac{v_0}{v}\right)^5. \tag{24}$$

Using Eqs. (1), (2), (22), and (24), we can write

$$\alpha_{att} = \alpha_0(1 - \phi)^{\beta-5(\kappa-\delta)}[\Re\{(1 - b\phi)^{1/2}\}]^5. \tag{25}$$

This gives the porosity dependence of the Akhiezer damping in PSi. The room temperature attenuation coefficient of bulk Si at 1 GHz is given in Table II. To use in Eqs. (12) and (16), the attenuation coefficient must be in nepers per unit length[59] such that $\alpha(\mathrm{Np/cm}) = \alpha(\mathrm{dB/cm})\frac{\ln 10}{20}$. The extinction coefficient, corresponding to the attenuation via the Akhiezer damping, can be expressed as

$$\varepsilon = \varepsilon_0(1-\phi)^{\beta-4(\kappa-\delta)}[\Re\{(1-b\phi)^{1/2}\}]^4. \quad (26)$$

2. Multiple scattering

In the limit of $ka < 1$, the acoustic losses due to the multiple scattering by voids are defined[30] by the imaginary part of the term, whose real part is given in Eqs. (2), (25), and (26)

$$\alpha_{sca} = k_1\,\Im\{(1-b\phi)^{1/2}\}. \quad (27)$$

IV. RESULTS AND DISCUSSION

A. Characteristics of the structures

Pairs of layers in the structures were designed to form a halfwave thick layer for ~0.6 GHz longitudinal acoustic waves. The measured average thicknesses were $d_A = 1.67\ \mu$m and $d_B = 2.37\ \mu$m for the BS and $d_A = 1.82\ \mu$m and $d_B = 2.33\ \mu$m for the FS. These thicknesses were used as fixed parameters in the simulation. Overall thicknesses for the BS and the FS were ~109 μm and ~115 μm, respectively.

The thicknesses, the characteristic impedances, and the acoustic velocities for longitudinal waves in the layers of the fabricated structures and the position and width of the fundamental Bragg gap are given in Table III. Note, $f_{Br}^{(1)}$ and $\Delta f_{Br}^{(1)}$ given in Table III for the FS are the center frequency and the width, respectively, of the fundamental gap of the *periodic* structure having the constitutive layers as the fabricated FS.

B. Acoustic transmission spectra

Figure 3 demonstrates the ATS measured for the BS and the FS on Si substrates described in Secs. I and II. The result of modelling all the layers in the system, including transducers, fluid, and substrate (see Figure 2), is also shown in Figure 3.

For the BS, in Figure 3(a), the band gaps at 0.63 and 1.86 GHz have a depth of ~60 dB, which is less than the modeled 150 dB. It was not possible to experimentally verify the predicted 150 dB attenuation for several reasons, which must be clarified in future work. One reason could be the fact that our experimental setup was measuring its sensitivity floor, shown in Figure 3(a) by a dashed green line. However, we see a truncated gap also in the cases when the experimental system is not yet hitting its noise floor. A small deviation from normal incidence can cause truncation of the gap due to the conversion of longitudinal and transverse modes. This deviation can be not only from imperfection in alignment of the transducers but also from the fact that the experimental coupling of the acoustic waves between the transducers varies from the idealised model of plane waves. In addition, wider and shallower gaps can appear due to the unintended variation of the target thickness and porosity of the etched layers (the gaps of higher order are more sensitive to this variation). There is also some discrepancy between theory and experiment, which comes from the correction procedure for the combined response of both transducers.

Thus, we can conclude that the stop bands have a depth of at least 50 dB for the 1st and 3rd order gaps at 0.63 and 1.88 GHz, respectively, and 30 dB and 20 dB for the 2nd and 4th order gaps at 1.26 GHz and 2.51 GHz, respectively. The existence of the 2nd and 4th order gaps show that the BS is not balanced ($t_A \neq t_B \neq 1/4f_{Br}$). The 4th gap is not well pronounced since the efficiency of the used transducers is very low in this region. The fine features of the spectrum are not noise but the side lobes from the whole structure with an overall thickness of ~109 μm, plus longitudinal modes from the Si pillars of the transducers (~520 μm) and the bulk Si substrate (~410 μm) (see Figure 2).

For the FS, in Figure 3(b), the gaps at 0.45 and 0.76 GHz have a depth of ~50 dB which, again, is less than the modeled value of 120 dB for the reasons mentioned above. These two deeper gaps are accompanied by two shallower gaps at 0.25 and 0.95 GHz. The gaps about 1.8 GHz are as well pronounced as corresponding 3-rd order gap of BS. The gaps at 1.2 and 2.4 GHz are weaker than the dominant gaps similar to the 2nd and 4th gaps of the BS in Figure 3(a).

TABLE III. Characteristics of the fabricated BS and FS.

	d_A (μm)	d_B (μm)	v_A (km/s)	v_B (km/s)	Z_A (MRayl)	Z_B (MRayl)	$f_{Br}^{(1)}$ (MHz)	$\Delta f_{Br}^{(1)}$ (MHz)
BS	1.67	2.37	4.46	5.62	10.38	13.09	628	249
FS	1.82	2.33	4.31	5.69	10.03	13.24	600	283

C. Acoustic losses

Acoustic losses such as attenuation and scattering by voids, and interface and surface roughness were included into the calculation. This results in the slope in the baseline of the ATS with reduced contrast of interference fringes (see Figure 3). The systematic experimental investigation of acoustic losses in PSi multilayers was not within the scope of the present work and future study is needed. We only note that the roughness of PSi surface is small (~1 nm) and has negligible contribution (<1%) to the scattering losses.[65,66] The roughness of interfaces between layers etched in the wafers of high doping level as used in our work is also small (2–5 nm). The interface between the porous layer and the substrate has been found slightly more rough ($\sigma \sim 5$–15 nm).[66,67] The main contribution to interface losses comes in our case from the unpolished back side of the substrate with σ of 50–700 nm.[68] The backside roughnesses of 100 nm and 350 nm were used for fitting the BS and FS spectra, respectively. The losses from viscous damping and multiple scattering by pores were included as described in

Sec. III F. The thickness of the coupling liquid layer was ~1 μm for the BS and ~40 μm for the FS.

D. Chirp

The target high and low porosity values were $\phi_A = 0.62$ and $\phi_B = 0.47$. Porosity is difficult to estimate from SEM pictures because charging affects the contrast profile.[9] Therefore, the porosity values were refined by fitting the experimental data. The best fit (see Figure 3) for the measured spectra gave porosity of $\phi_A = 0.67$ and $\phi_B = 0.50$ for the BS and $\phi_A = 0.69$ and $\phi_B = 0.49$ for the FS. These values were slightly higher than nominally planned.

Etching of relatively thick PSi structures, such as ours, is difficult due to the depletion of the etchant resulting in variation in the etch rate. This, in turn, results in a gradient—not necessarily linear—in both the porosity and thickness of the layers across the structure. This gradient is known as chirp. It is larger in high porosity layers due to the larger etching current and the consequent rapid depletion of the etchant. The chirp can be mitigated by implementing etch-stops during the etching process or by applying corrections to the etch current and duration time for each layer. The latter method was used in our case. Consequently, the layer thicknesses, as mentioned above in Sec. II, revealed no chirp in SEM measurements. The maximum uncontrolled porosity gradient over the structure was less than 3% and 7% for low and high porosity, respectively. Uncertainty in κ affects simulation in a similar way to uncertainty in ϕ as mentioned above in Sec. III A. Therefore, the deviation of the actual porosity from the nominal values may be smaller than obtained in simulations if κ is varied. However, at fitting, we decided to use a constant κ of 0.585, varying porosity ϕ instead. Thus, the positive chirp of porosity was included into the simulation implicitly by using averaged porosity for all layers of the same type in the structure. Although neither disorder nor chirp of thickness was included in simulation, a good agreement between the modelled and measured spectra is seen.

E. Folded phonons

The Brillouin zone folded dispersion curve for the real part of k calculated using Eq. (11) is shown in Figure 3(a). Attenuation was not included. The curve is in full agreement with the experimental spectrum and with the spectrum calculated using the transfer matrix method.

F. Balanced structures

In Figure 4(a), we demonstrate simulated spectra for BS (28 pairs) and FS ($L = 7$) where $t_A = t_B = 1/4f_{Br}$. The porosity and, thus, the velocity and impedance mismatch of the layers are the same as for the fabricated FS (see Table III). The layer thicknesses are modified to fulfil the relation $d_A/v_A = d_B/v_B$ keeping the gap frequency $f_{Br}^{(1)}$ the same as before, i.e., 0.6 GHz. The new thicknesses were calculated as: $d_A = v_A/4f_{Br}^{(1)}$ and $d_B = v_B/4f_{Br}^{(1)}$ and were 1.792 μm and 2.367 μm, respectively.

The amount of AB-pairs in the simulated BS is chosen to be 28 to keep the same overall thickness as for the simulated FS: ~116 μm. The small variation of overall thickness results mainly in small variation in spacing between the interference fringes (side lobes) of the ATS. This does not affect either the width or position or depth of the forbidden gaps. Those are defined by the impedance mismatch, the thickness of individual layer (A and B) and the number of AB-pairs in the structure according to Eqs. (4), (5), and (7).

The losses and the effects of transducers and substrate were not included in the calculation. Note that the frequency range of the ATS in Figure 4(a) is wider than in Figure 3 and the spectrum is plotted in dimensionless units $f/f_{Br}^{(1)}$.

It is seen from Figure 4(a) that, for the balanced structures, the even-order gaps have completely vanished and the odd-order gaps have become uniform in width and depth as predicted. In the FS, the gaps occur symmetrically about the BS gap frequencies. The deepest gaps of the FS are shallower and narrower than the corresponding gaps of the BS of the same overall thickness. Peaks with transmittance approaching unity (i.e., 0 dB) are seen between these FS gaps, and are similar to the mid-gap defect transmitting lines (defect states introduced when a periodic system is perturbed by a defect element) in the ATS of microcavities.[6,8] The position of the mid-gap transmission line of the microcavity is rather sensitive to the cavity phase length. On the contrary, the position of the transmission lines between FS gaps is more robust to dimensional change because it is the result of the whole FS structure. In the case of an unbalanced structure, however, the FS gaps distributed about the BS gap become asymmetric in intensity (see Figure 5(a)).

G. "Quasi-Fibonacci" periodic structures

It is shown in Figure 4(b) that the periodic BS constructed from 19 A^*B^* pairs, where $A^* = \{A\}$ and $B^* = \{BB\}$, thus $t_{B^*} = 2t_{A^*}$, roughly mimics the FS$|_{L=7}$. The better approximation of the FS can be achieved by the BS with $A^* = \{ABABB\}$ and $B^* = \{ABABBABB\}$. This can be useful for rough estimation of properties of the FS using the tools which exploit periodicity.

H. Unbalanced structures

In Figure 5(a), we demonstrate the simulated ATS for the FS ($L = 7$) and the BS (27 pairs) with $t_A \neq t_B$. The thicknesses $d_A = 1.45$ μm and $d_B = 2.82$ μm are arbitrary and chosen to make the layers strongly unbalanced with t_A and t_B not being integer multiples of each other, but keeping the gap position the same as before: $f_{Br}^{(1)} = 0.6$ GHz. The transmittance in the center frequency of the odd and the even-order BS gaps is depicted in Figure 5(a) by the guiding lines. It is seen that the increase of the depths of the BS gaps is strongly correlated with the increase of the gap widths according to Eq. (5) with oscillatory behaviour with a half-period of $2t/t'$, which goes to infinity for $t' = 0$. In the FS, the gaps spanned around the BS gap of the order m are asymmetric about the center frequency of the BS gap, as mentioned above, and some gaps almost completely disappear. Nevertheless, the combined depth of the FS gaps is correlated with the depth of the corresponding BS gaps.

In Figure 5(b), the correlation between widths and depths of the BS gaps from Figure 5(a) is demonstrated. As

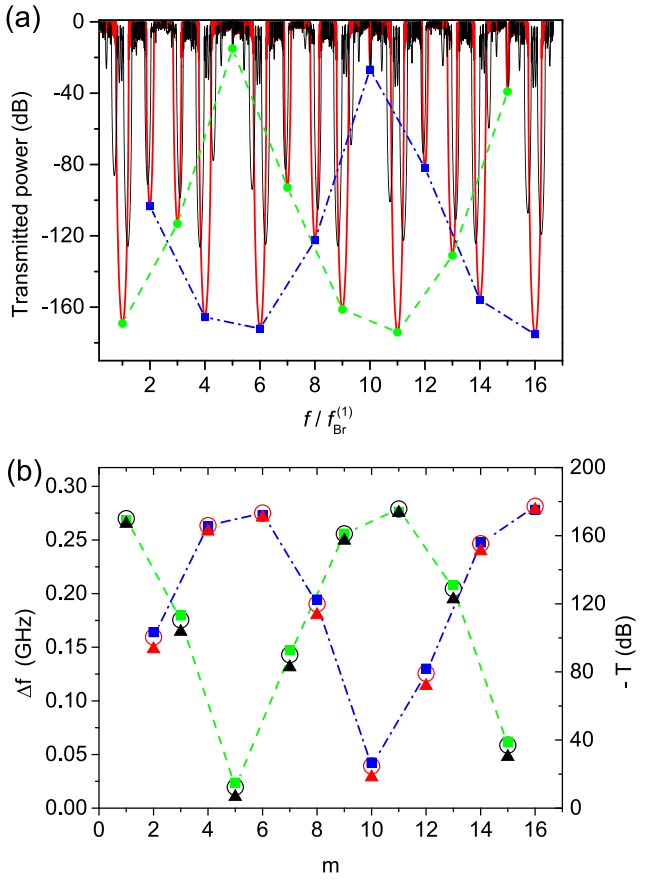

FIG. 5. (a) The simulated ATS of the BS (27 pairs), thick red line, and the FS (L = 7), thin black line. Porosity of the layers is the same for the BS and FS: $\phi_A = 0.69$ and $\phi_B = 0.49$, as in Figure 4. The thicknesses are: $d_A = 1.45\,\mu$m and $d_B = 2.82\,\mu$m. The transmittance in the center frequency of the odd (even) order BS gaps is depicted by the circles (squares) and guided by the dashed line. (b) Correlation between the gap width and the gap depth. Left scale, open circles: the gap width calculated using Eq. (5). Right scale: the transmittance in the center frequency of the gaps obtained from the numerical simulation (close squares) and calculated using Eq. (8) (close triangles). The odd and the even gaps are guided by the dashed (green) and the dash-dot (blue) lines, respectively.

it is seen from Figure 5(b), Eq. (8) gives a good approximation for gap depths in the ATS of an unbalanced BS.

V. CONCLUSIONS

This work provides experimental verification of the acoustic transmission properties of one-dimensional quasi-periodic Fibonacci and periodic phononic crystals fabricated in porous silicon. Transmission spectra for hypersonic longitudinal phonons propagating perpendicularly to the interface have been recorded. These spectra exhibit phononic gaps with more than 50 dB depth (measurement is limited by the accuracy of the experimental system).

The layers were consecutively electrochemically etched into highly boron doped (100)-Si wafers. Throughout the overall thickness of about 110 μm, the layers were etched almost without chirp in thickness and with moderate chirp in porosity.

The spectra were simulated using the transfer matrix method. It has been shown that at normal incidence of acoustic waves, the optical methods can be used for simulation of acoustic wave propagation through a multilayered structure. By just changing a scaling factor, acoustic devices can be designed in the same way as optical devices. However, the important difference—the acoustic velocity dependence on porosity—must be considered in designing acoustic devices. The formula describing velocity dispersion via multiple scattering by voids has been given (Eq. (2)). The formula is consistent with the one commonly used in the literature.

It has been shown that, as result of the proportionality of elastic constants as a function of porosity, the averaged Grüneisen parameter for porous silicon is constant. The constant Grüneisen parameter simplifies the formula for porosity dependence of the Akhiezer damping (Eq. (25)).

The periodic and quasi-periodic structures consisting of layers which are not quarter-wavelength have been simulated and analyzed. Special cases when the path-length of one layer is an integer multiple of the second layer have been analyzed. Gaps of certain orders will collapse in these cases.

An analytical expression approximating the relation between the widths and the depths of forbidden gaps in unbalanced periodic structures has been suggested (Eq. (8)). Good agreement with the numerically simulated data has been demonstrated.

The natural Fibonacci-like sequences for calculating the number of B' and B'' type layers in Fibonacci structure have been given (Table I).

Periodic structures mimicking quasi-periodic Fibonacci structure have been simulated.

We hope that the methods described here will be of assistance in the further development of both periodic and non-periodic phononic devices working in the hypersonic region, especially those fabricated from PSi and similar porous materials.

ACKNOWLEDGMENTS

We thank U. Potter for help in SEM cross-section measurements, S. J. Bingham for very useful discussions, and J. J. Davies for helpful comments.

APPENDIX: SAYER'S COEFFICIENTS

$$A = 2 - \frac{3}{4}\xi^2 + 5\left(1 - \frac{9}{4}\xi^2\right)^{-1},$$

$$B = -\frac{16}{15} + \frac{5}{12}\xi^2 - \frac{3}{16}\xi^4 + \frac{7}{15}\left(1 - \frac{19}{12}\xi^2\right)^{-1} - \frac{5}{9}\left(5 - \frac{9}{4}\xi^2\right)\left(1 - \frac{9}{4}\xi^2\right)^{-2},$$

$$C = \frac{4}{9} - \frac{1}{2}\xi^2 + \frac{2}{9}\xi^3 + \frac{3}{16}\xi^4 + \frac{5}{3}\left(1 - \frac{9}{4}\xi^2\right)^{-2}\left(1 + \frac{3}{2}\xi^5\right),$$

$$\xi = v_L/v_S.$$

[1]W. Steurer and D. Sutter-Widmer, J. Phys. D: Appl. Phys. **40**, R229 (2007).

[2]S. Mahon and R. Aigner, CS MANTECH Conference, May 14-17, Austin, Texas, USA, 2007.
[3]E. Maciá, Rep. Prog. Phys. **75**, 036502 (2012).
[4]X.-H. Deng, J.-T. Liu, J.-H. Huang, L. Zou, and N.-H. Liu, J. Phys.: Condens. Matter **22**, 055403 (2010).
[5]K. S. Pérez, J. O. Estevez, A. Méndez-Blas, J. Arriaga, G. Palestino, and M. E. Mora-Ramos, Nanoscale Res. Lett. **7**, 392 (2012).
[6]P. D. C. King and T. J. Cox, J. Appl. Phys. **102**, 014902 (2007).
[7]L. C. Parsons and G. T. Andrews, Appl. Phys. Lett. **95**, 241909 (2009).
[8]G. N. Aliev, B. Goller, D. Kovalev, and P. A. Snow, Appl. Phys. Lett. **96**, 124101 (2010).
[9]L. Thomas, G. N. Aliev, and P. A. Snow, Appl. Phys. Lett. **97**, 173503 (2010).
[10]G. N. Aliev, B. Goller, P. A. Snow, H. Heinrich, B. Yuan, and R. Aigner, Nanoscale Res. Lett. **7**, 378 (2012).
[11]G. N. Aliev, B. Goller, and P. A. Snow, J. Appl. Phys. **110**, 043534 (2011).
[12]R. Nava, J. A. del Río, J. C. Alonso, and C. Wang, Engineered Porosity for Microphotonics and Plasmonics (Mater. Res. Soc. Symp. Proc., 2004), Vol. 797, pp. W5.2.1.
[13]V. Agarwal and M. E. Mora-Ramos, J. Phys. D: Appl. Phys. **40**, 3203 (2007).
[14]V. Agarwal, M. E. Mora-Ramos, and B. Alvarado-Tenorio, Photonics Nanostruct. Fundam. Appl. **7**, 63 (2009).
[15]R. Nava, J. Tagüeña-Martínez, J. A. del Río, and G. G. Naumis, J. Phys.: Condens. Matter **21**, 155901 (2009).
[16]L. Dal Negro, C. J. Oton, Z. Gaburro, L. Pavesi, P. Johnson, A. Lagendijk, R. Righini, M. Colocci, and D. S. Wiersma, Phys. Rev. Lett. **90**, 055501 (2003).
[17]V. Lehmann, *Electrochemistry of Silicon* (Wiley-VCH, Weinheim, 2002).
[18]V. Torres-Costa and R. J. Martín-Palma, J Mater. Sci. **45**, 2823 (2010).
[19]V. Yu. Timoshenko, L. A. Osminkina, A. I. Efimova, L. A. Golovan, P. K. Kashkarov, D. Kovalev, N. Künzner, E. Gross, J. Diener, and F. Koch, Phys. Rev. B **67**, 113405 (2003).
[20]W. Pabst, E. Gregorová, and G. Tichá, J. Eur. Ceram. Soc. **26**, 1085 (2006).
[21]G. Mavko, T. Mukerji, and J. Dvorkin, *The Rock Physics Hand-book* (Cambridge University Press, Cambridge, 2003).
[22]A. K. Maitra and K. K. Phani, J. Mater. Sci. **29**, 4415 (1994).
[23]J. A. Ogilvy, *Theory of Wave Scattering from Random Rough Surfaces* (Adam Hilher, Bristol, Philadelphia, New York, 1991).
[24]I. Filinski, Phys. Status Solidi B **49**, 577 (1972).
[25]J. Szczyrbowski and A. Czapla, Thin Solid Films **46**, 127 (1977).
[26]C. L. Mitsas and D. I. Siapkas, Appl. Opt. **34**, 1678 (1995).
[27]G. Lérondel and R. Romestain, Appl. Phys. Lett. **74**, 2740 (1999).
[28]P. C. Waterman and R. Truell, J. Math. Phys. **2**, 512 (1961).
[29]R. Truell, C. Elbaum, and B. B. Chick, *Ultrasonic Methods in Solid State Physics* (Academic, New York, 1969).
[30]C. M. Sayers, J. Phys. D: Appl. Phys. **14**, 413 (1981).
[31]M. Krüger, S. Hilbrich, M. Thönissen, D. Scheyen, W. Theiß, and H. Lüth, Opt. Commun. **146**, 309 (1998).
[32]M. S. Salem, M. J. Sailor, F. A. Harraz, T. Sakka, and Y. H. Ogata, J. Appl. Phys. **100**, 083520 (2006).
[33]D. Bellet, P. Lamagnère, A. Vincent, and Y. Bréchet, J. Appl. Phys. **80**, 3772 (1996).
[34]S. Tamura and J. P. Wolfe, Phys. Rev. B **36**, 3491 (1987).
[35]Agilent Network Analyzer Basics [http://cp.literature.agilent.com/litweb/pdf/5965-7917E.pdf], Agilent Technologies, Inc., USA, 2004, 5965-7917E: 1–94.
[36]P. Granitzer and K. Rumpf, Materials **3**, 943 (2010).
[37]G. N. Aliev, B. Goller, D. Kovalev, and P. A. Snow, Phys. Status Solidi C **6**, 1670 (2009).
[38]A. M. Polomska-Harlick and G. T. Andrews, J. Phys. D: Appl. Phys. **45**, 075302 (2012).
[39]Z. Lazcano, J. Arriaga, and G. N. Aliev, J. Appl. Phys. **115**, 154505 (2014).
[40]R. J. M. Da Fonseca, J. M. Saurel, A. Foucaran, J. Camassel, E. Massone, T. Taliercio, and Y. Boumaiza, J. Mater Sci. **30**, 35 (1995).
[41]H. J. Fan, M. H. Kuok, S. C. Ng, R. Boukherroub, J.-M. Baribeau, J. W. Fraser, and D. J. Lockwood, Phys. Rev. B **65**, 165330 (2002).
[42]H.-Y. Hao and H. J. Maris, Phys. Rev. Lett. **84**, 5556 (2000).
[43]H.-Y. Hao and H. J. Maris, Phys. Rev. B **63**, 224301 (2001).
[44]P. V. Santos, L. Ley, J. Mebert, and O. Koblinger, Phys. Rev. B **36**, 4858 (1987).
[45]P. H. Lissberger, Rep. Prog. Phys. **33**, 197 (1970).
[46]S. M. Rytov, Sov. Phys. Acoust. **2**, 68 (1956).
[47]S. Tamura, D. C. Hurley, and S. Wolfe, Phys. Rev. B **38**, 1427 (1988).
[48]S. Mizuno and S. Tamura, Phys. Rev. B **45**, 734 (1992).
[49]L. M. Brekhovskikh and O. A. Godin, *Acoustics of Layered Media I*, 2nd ed. (Springer-Verlag, Berlin, Heidelberg, New York, London, Paris, Tokio, Hong Kong, 1999).
[50]M. O. Culjat, R. S. Singh, S. N. White, R. R. Neurgaonkar, and E. R. Brown, Acoust. Res. Lett. Online **6**, 125 (2005).
[51]A. Briggs, *Acoustic Microscopy* (Clarendon Press, Oxford, 1992).
[52]H. J. McSkimin and P. Andreatch, Jr., J. Appl. Phys. **35**, 2161 (1964).
[53]G. M. B. Webber and R. W. B. Stephens, *Physical Acoustics, IVB* (Academic Press, New Yourk, 1968).
[54]W. P. Mason and T. B. Bateman, J. Acoust. Soc. Am. **36**, 644 (1964).
[55]P. Emery and A. Devos, Appl. Phys. Lett. **89**, 191904 (2006).
[56]D. H. R. Price and C. D. W. Wilkinson, Appl. Phys. Lett. **16**, 480 (1970).
[57]M. J. S. Low, IEEE Trans. Ultrason., Ferroelectr., Freq. Control. **42**, 525 (1995).
[58]S. I. Rokhlin and L. Wang, J. Acoust. Soc. Am. **112**, 822 (2002).
[59]B. A. Auld, *Acoustic Fields and Waves in Solids* (Krieger Publishing Company, Malibar, Florida, 1990), Vol **1**.
[60]S. D. Lambade, G. G. Sahasrabudhe, and S. Rajagopalan, Phys. Rev. B **51**, 15861 (1995).
[61]R. Nava, M. P. Vecchi, J. Romero, and B. Fernandez, Phys. Rev. B **14**, 800 (1976).
[62]S. Lettieri, U. Bernini, E. Massera, and P. Maddalena, Phys. Status Solidi C **2**, 3414 (2005).
[63]V. N. Belomestnykh, Tech. Phys. Lett. **30**, 91 (2004).
[64]K. Leont'ev, Sov. Phys. Acoust. **27**, 309 (1981).
[65]G. Lérondel, R. Romestain, F. Madéore, and F. Muller, Thin Solid Films **276**, 80 (1996).
[66]C. Faivre and D. Bellet, J. Appl. Crystallogr. **32**, 1134 (1999).
[67]G. Lérondel, R. Romestain, and S. Barret, J. Appl. Phys. **81**, 6171 (1997).
[68]Y.-P. Zhao, I. Wu, C.-F. Cheng, U. Block, G.-C. Wang, and T.-M. Lu, J. Appl. Phys. **84**, 2571 (1998).